UNIVERSITÀ DI TRENTO

Dipartimento di Fisica

NANOSCIENCE LABORATORY HIGHLIGHTS 2020

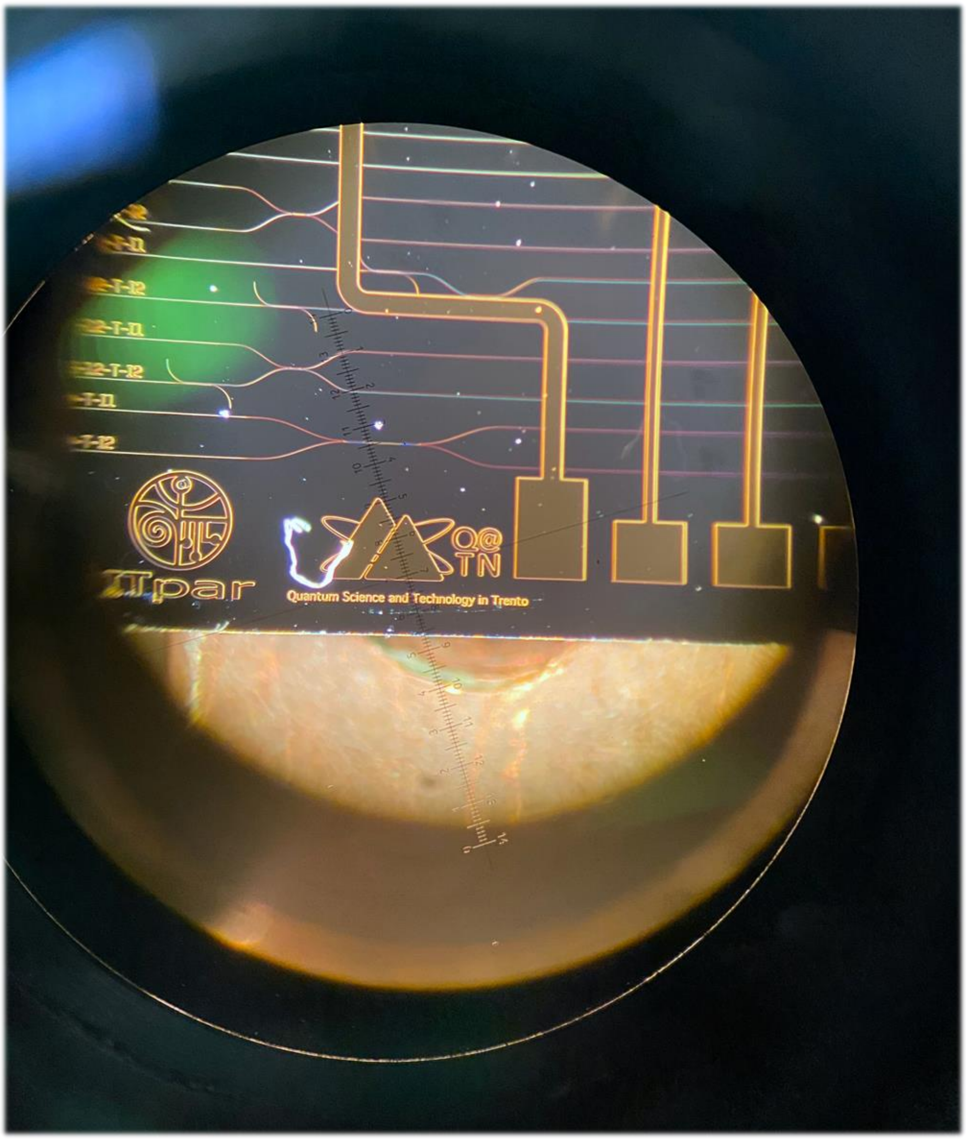

Image on the front cover: *Photograph of a silicon nitride chip for single particle entangled photon generation*
(Courtesy of Nicolò Leone)

NANOSCIENCE LABORATORY

MEMBERS (2020)

Faculty staff
Lorenzo Pavesi (full professor, head)
Marina Scarpa (full professor)
Zeno Gaburro (associate professor)
Paolo Bettotti (associate professor)
Stefano Azzini (assistant professor)
Mattia Mancinelli (researcher)
Beatrice Vignoli (researcher)

Technical staff
Enrico Moser
Giorgio Fontana
Elvira D'Amato

Post-docs
Stefano Signorini
Stefano Biasi
Massimo Borghi
Ilya Auslender

Administrative staff
Chiara Rindone

Doctoral students
Stefano Biasi (left April 2020)
Sara Piccione (left July 2020)
Chiara Vecchi
Clara Zaccaria
Davide Bazzanella
Nicolò Leone
Riccardo Franchi
Dhouha Jemmelli
Giovanni Donati
Matteo Sanna
Johanna Mae Indias

Master students
Federico Baldi
Nicola Bianchi
Matteo Sanna

SCIENTIFIC MISSION

Introduction to the Nanoscience Laboratory

The Nanoscience Laboratory (NL) is one of the scientific groups of the Department of Physics, University of Trento. Its main areas of research are neuromorphic photonics, integrated quantum photonics, linear and nonlinear silicon photonics and nanobiotechnologies. The mission of NL is to generate new knowledge, to develop understanding and to spin-off applications from physical phenomena associated with photons and their interactions with matter, particularly when it is nanostructured. Specifically, NL aims at understanding the optical properties of ligthwave systems such as optical waveguides, microresonators and complex dielectric systems. NL covers the whole value chain from fundamental phenomena to device applications, where the photonic platform is compatible with the main driving silicon microelectronic technologies. However, silicon is not the only material studied. Other fields of interest concern the use of cellulose to tailor the properties of nanostructure atom-by-atom or the use of perovskites to investigate their new properties.
NL research group consists of more than 25 people with different scientific backgrounds. Researchers from physics, physiology, bio-chemistry, materials science and electrical engineering are gathered to form a group of interdisciplinary nature. It is worth mentioning that NL collaborates closely with the Center of Materials and Microsystems, Fondazione Bruno Kessler (FBK). This collaboration spans over the last thirty years and covers various topics such as fabrication, testing and application of biomaterials and silicon based devices. Both participate in many common projects. The current ones are: projects LESSO, NEMO, QRANGE and Q@TN. A new strategic collaboration is ongoing with the Trento units of CNR-INO, specifically dedicated to implement topological effects in integrated silicon chip. Moreover, with the support of FBK and CNR and every odd year, NL organizes a winter school on optoelectronics and photonics. The 10th edition was organized on "Nonlinear Photonics" (20-26 January, 2019) and the 11th edition will be on "Neuromorphic Photonics" in june 2021. Furthermore, the members of NL are often invited to participate in the organizing committees of international conferences or workshops.
The research activities of NL are mainly supported by the local government (PAT), by the European Commission, by the Italian Ministry of Education, University and Research (MIUR) and by companies. During the period covered by these Highlights, NL has been and is involved in the following projects: PRIN-MIUR 2015 NEMO "Nonlinear dynamics

of optical frequency combs"; PRIN-MIUR 2017 PELM "Photonics Extreme Learning Machine: from neuromorphic computing to universal optical interpolant, strain gauge sensor and cancer morphodynamic monitor"; PRIN-MIUR 2017 PANACEA "A technology PlAtform for the sustainable recovery and advanced use of NAnostructured CEllulose from Agri-food residues"; ERC-2017-ADG-788793 BACKUP: "Unveiling the relationship between brain connectivity and function by integrated photonics"; ERC-POC ALPI "optical signal recovery by Photonic neural network Integrated in a transceiver module"; H2020-FETFLAG-2018-03 QRANGE: "Quantum Random Number Generators: cheaper, faster and more secure"; H2020-FET H2020-FETOPEN-2018-2019-2020-01 EPIQUS "Electronic-photonic integrated quantum simulator platform"; Q@TN project "Quantum Science and Technology in Trento"; India-Trento Program for Advanced Research - ITPAR: "A cheap, light, compact source for QKD based on intraparticle entanglement in an integrated photonic circuit"; ASI - LESSO: "Laser etero-integrato a stato solido per trappole ottiche"; NANOFARM (Legge Provinciale 13 dicembre, 1999 n. 6).

Silicon Nanophotonics

Silicon photonics is the technology where photonic devices are produced by standard microelectronic processes using the same paradigm of electronics: integration of a large number of devices to yield a high circuit complexity, which allows for high performances and low costs. Here, the truth is to develop photonic devices that can be easily integrated to improve the single device performance and to allow high volume production.
In the next year, we will mostly concentrate on two alternative approaches where photonics is used to compute. On one side, we will develop new scheme to implement artificial intelligent in a photonic silicon chip by using brain-inspired or neuromorphic computing schemes. On the other side, we will use silicon photonics to provide a suitable platform for quantum computing and quantum simulations. In both approaches one fundamental device is the silicon microresonator where whispering gallery modes induce nonlinearities which can be exploited to generate new quantum states of light or to realize recurrent neural network. In addition, we use micro-disks or micro-rings to study new physics (chirality, frequency comb generation, entangled photon generation). The microresonators are coupled directly with narrow mode SOI (Silicon-on-Insulator) waveguides. Also, multimode waveguides are used for nonlinear frequency conversion or generation.
To develop silicon photonics, one further add-on is making silicon to do something that it is not able to do in its standard (bulk) form. Low dimensional silicon, where small silicon nanocrystals or nanoclusters (Si-nc) are developed, is one way to compel silicon to act as an active optical material. Alternatively, we use the built-in or p-i-n induced electric fields to tune the non-linear optical properties of silicon waveguides for the development of new MIR sources (parametric generation via second order effects or frequency comb generation). Nonlinear optics is finally used to generate pairs of entangled photons, which in turn feed quantum interferometers or integrated quantum photonic circuits.
Lastly, hybrid chips are developed to interface living neurons with photonic waveguides in the search for artificial intelligence. Here, the signal transduction is achieved by using photo-sensitive proteins.

Advanced nanomaterials for energy, environment and life.

In this research activity, we learn from nature how to use molecules or biological nanostructures to build materials with specific features. The focus is on understanding the properties of colloids of biological origin, the dynamics at the bio-interfaces, the strength and stability of natural structures. The final goal is to transfer the acquired knowledge on innovation by developing sustainable and smart materials and processes.

Porous silicon nanotechnology

This research is focused on porous silicon nanotechnology, with emphasis on the physico-chemical properties (i.e. luminescence, surface effects) of this material, biocompatibility and *in vitro* drug delivery applications. In our Lab sponge-like luminescent mesoporous silicon microparticles are produced from crystalline silicon with a simple and cheap top-down fabrication process. These microparticles are stabilized by coating (with small coating molecules, polymers, inorganic shells) to preserve their photoluminescence, colloidal stability and increase their biocompatibility. These microparticles are then infiltrated with drugs and/or magnetic particles to be used in bioimaging or pharmaceutics.

Experimental facilities

The NL facilities allow for detailed experimental studies in nanoscience, photonics and biotechnologies. Since the effective collaboration with FBK most material processing and device productions are performed within their premises. For photonics, we have facilities to cover the light spectrum from the THz to UV ranges with whatever time resolution is needed. Laser sources comprehends: Ti-sapphire fs-ps laser (1 W average over 1000-700 nm, 2 ps or 70 fs pulses, 82 MHz repetition rate) interfaced with a second harmonic generator and pulse picker; TOPAS pumped with an amplified Ti:Sa laser which covers the 1-2.6 μm range with 35 fs, 10 kHz, 3 mJ; 2W tunable CW Cr:ZnSe/S fiber-bulk hybrid laser to cover the 2-3 μm range; four tunable CW lasers (850-870 nm, 1200 - 1700 nm and 1500 - 1600nm) fiber pig-tailed; high power fiber-laser at 1550 nm (1-100 MHz, 50 ps); 4W EDFA and 2W semiconductors amplifiers, a supercontinuum light source (410-2400 nm, 1W), several pig-tailed diode lasers, ASE source at 1550 nm and a broad band SLD at 800 nm; three high-power true-CW DPSS single-line laser operating at 532, 473 and 355 nm. Detectors comprehend: visible and infrared photomultipliers and CCDs, a visible streak camera with ps resolution, 4K cooled bolometers which cover THz region, avalanche photodiodes for vis and IR ranges plus many single photon detectors in the visible and IR. Two home-made MIR single photon-counters. To perform spectral analysis several setups are available: FTIR and dispersive spectrophotometers, a micro-Raman setup, a micro-FTIR and a UV-vis-IR spectrophotometer (shared with other laboratories), UV-Vis and fluorescence spectrophotometer dedicated to biochemical experiments. Eight set-ups are dedicated to the characterization of waveguides equipped with nanopositioning systems and polarization controllers, each specified on a given function: visible, visible broad range, quantum, passive infrared, high speed infrared, non-linear infrared, non-linear MIR and on wafer. A set-up is dedicated to high-speed measurements, with 80 Gbps capability where a 60 GHz arbitrary waveform generator, electro-optical modulators, coherent detectors and a four channels, 20 GHz oscilloscope. Other devices are: - a solar simulator for cells up to 5 inches in size; - two nanoprobe stations (AFM and SNOM) - two semiconductor probe stations (4 and 8 inches) and different electrical characterization systems (I-V, Z-Ω, EL-I, etc.). Four VIS to NIR optical spectrum analyzers are available. A probe station is interfaced by a fibres bundle with a spectrometer equipped with nitrogen cooled visible and IR CCDs. An electrochemical laboratory with various chemical hoods, galvanostats and volt-ameters is available for sample processing. For optical, electrical and molecular dynamics simulations, the laboratory uses free and commercial software and has three workstations. There are laboratories dedicated to chemical synthesis and to the preparation of biological samples. Two other laboratories with biological hoods, incubators and confocal microscopes are dedicated to biological experiments. In one, a confocal microscope with an insert for electrophysiology (MEA, multi electrode array) and optogenetics measurement equipped with a "spinning disk" system for fast acquisitions and a super-resolution system.

2020 Publications

- P. Guillemé, C. Vecchi, C. Castellan, S. Signorini, M. Ghulinyan, M. Bernard, M. Parisi and L. Pavesi, “Robust Geometries for Second-Harmonic-Generation in Microrings Exhibiting a 4-Bar Symmetry”, Appl. Sci. 2020, 10, 9047 (2020).
- M. Pasini, N. Leone, S. Mazzucchi, V. Moretti, D. Pastorello and L. Pavesi, “Bell-inequality violation by entangled single-photon states generated from a laser, an LED, or a halogen lamp “, Physical Review A 102, 063708 (2020).
- N. Leone, D. Rusca, S. Azzini, G. Fontana, F. Acerbi, A. Gola, A. Tontini, N. Massari, H. Zbinden, L. Pavesi, “An optical chip for self-testing quantum random number generation”, APL Photonics 5, 101301 (2020).
- S. Azzini, S. Mazzucchi, V. Moretti, D. Pastorello, L. Pavesi, “Single-Particle Entanglement”, Adv. Quantum Technol. 3, 2000014 (2020).
- Stefano Signorini and Lorenzo Pavesi, “On-chip heralded single photon sources”, AVS Quantum Sci. 2, 041701 (2020).
- C. Piotto, S. P. Pujari, H. Zuilhof and P. Bettotti, “Surface Heterogeneous Nucleation-Mediated Release of Beta-Carotene from Porous Silicon”, MDPI - Nanomaterials 10(9), 1659 (2020).
- Calabrese, F. Ramiro-Manzano, H. M. Price, S. Biasi, M. Bernard, M. Ghulinyan, I. Carusotto, and L. Pavesi, “Unidirectional reflection from an integrated “taiji” microresonator”, Photonics Research, Volume: 8, Issue: 8, Page 1333 (2020).
- F. Acerbi, N. Massari, L. Gasparini, A. Tomasi, N. Zorzi, G. Fontana, L. Pavesi and A. Gola, “Structures and Methods for Fully-Integrated Quantum Random Number Generators”, IEEE Journal of Selected Topics in Quantum Electronics, 26, 9200116 (2020).
- R. Franchi, C. Castellan, M. Ghulinyan and L. Pavesi, “Second-harmonic generation in periodically poled silicon waveguides with lateral p-i-n junctions”, Optics Letters, 45, 3188 (2020).
- C. Vecchi, C. Castellan, M. Ghulinyan, M. Bernard and L. Pavesi, “Electric field-induced second harmonic generation in silicon waveguide by interdigitated contacts”, Proc. SPIE 11364, Integrated Photonics Platforms: Fundamental Research, Manufacturing and Applications, 113640L (2020).
- S. Paesani, M. Borghi, S. Signorini, A. Maïnos, L. Pavesi and A. Laing, “Near-ideal spontaneous photon sources in silicon quantum photonics”, Nature Communications 11, 2505 (2020).
- S. Piccione and L. Pavesi, “Design of an external cavity semiconductor laser for intra-cavity beam combining”, Proc. SPIE 11266, Laser Resonators, Microresonators, and Beam Control XXII, 1126615 (2020).
- Chistè E, Ischia G, Gerosa M, Marzola P, Scarpa M, Daldosso N. Porous si microparticles infiltrated with magnetic nanospheres. Nanomaterials 2020;10(3).

2020 Patents

- DISPOSITIVO LASER A GUADAGNO INTERFEROMETRICO (inventori Sara Piccione, Stefano Biasi, Lorenzo Pavesi. IT Domanda N. 102020000001897 del 31 gennaio 2020)
- APPARATO DI PRODUZIONE DI FOTONI COMPRENDENTI STATI DI SINGOLO FOTONE IN CORRELAZIONE QUANTISTICA. (inventori Pavesi Lorenzo, Valter Moretti, Sonia Mazzucchi, Davide Pastorello, Matteo Pasini. IT Domanda N. 102020000005521 del 16 marzo 2020)
- OPTICAL APPARATUS (inventors Massimo Borghi, Stefano Signorini, Stefano Paesani, Lorenzo Pavesi. GB application number 2005827.7 del 21 aprile 2020)

2020 PhD Thesis:

- Stefano Biasi, "Light propagation in confined photonic structures: modeling and experiments" (22nd April 2020)
- Sara Piccione " Multi-gain interferometric laser for intra-cavity beam combining" (14th July 2020)

Project web sites

http://nanolab.physics.unitn.it/
https://r1.unitn.it/back-up/
https://r1.unitn.it/back-up/erc-poc-alpi-project/
https://epiqus.fbk.eu/
https://qrange.eu/
https://sites.google.com/view/prin-nemo/
https://sites.google.com/unitn.it/panacea/home
https://r1.unitn.it/pelm/
https://www.quantumtrento.eu/

1. Disorder effects on Electric Field Induced Second Harmonic Generation in an interdigitated poled silicon waveguide (Chiara Vecchi, Riccardo Franchi)

In the last decades, many efforts have been focused to induce nonlinear second order effects in silicon waveguide. Unfortunately, the second-order susceptibility $\chi^{(2)}$of silicon in the dipole approximation is suppressed due to its centrosymmetry. One way to achieve a $\chi^{(2)}$ in Si is by exploiting a third-order nonlinear effect, the Electric Field Induced Second Harmonic Generation (EFISHG). This phenomenon, through the use of a constant electric field (E_{DC}) within the waveguide generated by lateral p-i-n junctions, gives rise to a $\chi^{(2)}$ proportional to the electric field, $\chi^{(2)}_{EFISH} = 3\chi^{(3)}E_{DC}$. Poling can be used to achieve a quasi/phase matching condition so that a modulation of the susceptibility, $\Delta\chi^{(2)}_{EFISH}$, allows to conserve the photons momenta. Therefore, we engineered the poling geometry to amplify $\Delta\chi^{(2)}_{EFISH}$ using an *interdigitated* configuration. In this configuration, doped regions of different types are alternating along the waveguide length direction. We saw that using an *interdigitated* poling structure results in an increase of the generation efficiency, η by approximately ten times, compared to using a *simple* configuration (where one type of doping is realized on each side of the waveguide).

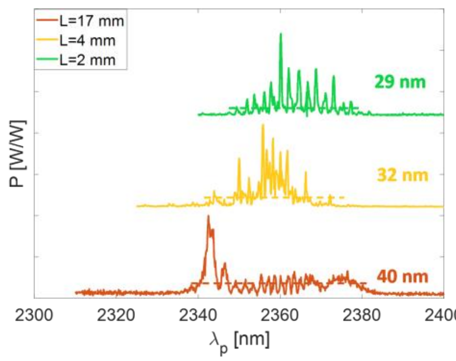

Figure 1: V*ariation of the emission band as a function of the waveguide length. The measurements have been done on the same 17 mm long waveguide before and after cleaving. $\lambda_p$is the pump wavelength*

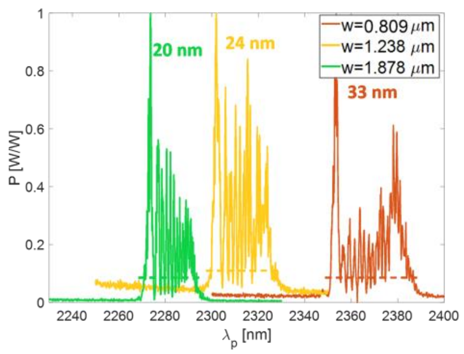

Figure 2: *Variation of the emission bandwidth as function of the width of the waveguide.*

Looking at the generation efficiency as a function of the pump wavelength, for different lengths of the same waveguide, L, we can see the presence of a generation band about 10nm wide at $L = 17$mm, much larger than the theoretical prediction of 2nm. Furthermore, decreasing the length of the waveguide the generation bandwidth decreases (Fig. 1) and increasing the width of the waveguide the generation band decreases (Fig. 2). This behavior is given by the presence of unwanted fluctuations in the geometry of the waveguide. The generated power P_{SH} in SHG can be written as $P_{SH} = P_p^2\left|\tilde{\gamma}^{(2)}_{SH}\right|^2 L^2 S$ with S defined as $S = \frac{1}{L^2}\left|\int_0^L s(z)e^{i\Delta\beta z}\right|^2$ and L is the waveguide length. S shows a dependence on $\Delta\beta$, which is the mismatch function between the SH and pump wave vectors and has a strong dependence from the waveguide geometry. The presence of these fluctuations has been modeled. Introducing random fluctuations over the width of the waveguide we saw the broadening of the window in which SH can be generated caused by the widening of the phase matching region. Performing simulations using a standard deviation $\sigma_w = 3$nm over the waveguide width and taking into account that the generation length L is not the total length of the waveguide ($L = 17$mm) but the coherence length of the source ($L_{coh} = 6$mm), we obtained the same generation bandwidth and we reproduced the main features of η spectrum, as shown in Fig. 3. It is important to notice that being random fluctuations it is not possible to fit all the different peaks.

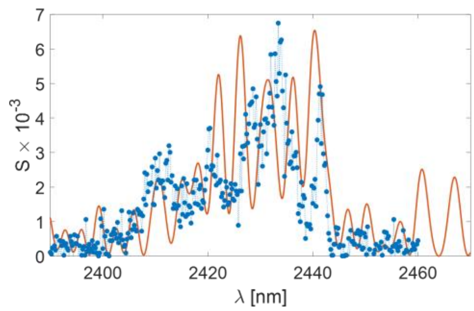

Figure 3: *real spectrum of an interdigitate poling configuration waveguide (red) compared with the results of a simulation (black)*

2. Robust Geometries for Second-Harmonic-Generation in Microrings Exhibiting a 4-Bar Symmetry (Chiara Vecchi)

In 2015, optical frequency comb generation has been demonstrated in silicon microring resonators by using four wave mixing and self-phase modulation. Due to these nonlinear processes, the frequency comb generation was limited in its frequency span. To extend this span beyond one octave, the use of second-order nonlinearities is suggested. Microring resonators made of materials with a diamond lattice, such as silicon, allow exploiting a 4-bar symmetry to achieve quasi-phase matching for second-order optical nonlinearities. However, fabrication tolerances impose severe limits to the quasi-phase matching condition, which in turn degrades the generation efficiency. Therefore, we developepd a method to mitigate these limitations. As a model, we study SHG in a Si microring with waveguide width w, waveguide thickness e and internal microring radius R_{in}. The pump field is coupled to the microring by a bus waveguide, which is also used to collect the second harmonic field.

In order to have SHG in the ring, we look for a geometry that can support in a resonant way both the pump as well as the SH. By COMSOL simulation we computed the relationship between the internal radius and the thickness values which fulfill the SHG condition (Fig. 4). The curve has a flat maximum around $e = 330$ nm. This peculiarity can be used to overcome the effect of the fabrication imperfection that degrade the efficiency of the process.

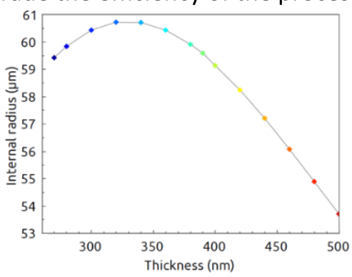

Figure 4: *Microring internal radius as function of the waveguide thickness.*

The computed conversion efficiency $\eta = P_{SH}/P_p^2$ is shown in Fig. 5. A weak dependence on the geometrical parameters is observed for the optimal geometry represented by the green curve.

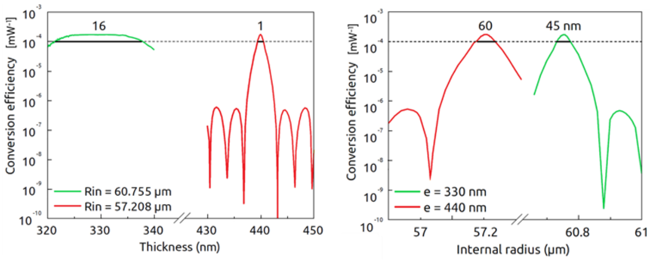

Figure 5: *Conversion efficiency as function of the waveguide thickness (left) and conversion efficiency as function of the microring internal radius (right). The green curve is the curve relative to the maximum of the curve shown in* Fig. 2 *while the red curve is relative to a point far away from this flat region.*

As the only requirement to find the conversion efficiency expression is the geometry of the second order susceptibility, the method can be easily transferred to other material systems showing a 4-bar symmetry of the crystalline structure.

3. Nonlinearity-Induced reciprocity breaking in a Taiji microresonator (Stefano Biasi, Riccardo Franchi)

In the last decade, several efforts have been made to develop unidirectional optical circuits, which show different responses depending on the direction of the incident light. The realization of an integrated optical system, capable of working as an isolator in the linear regime, is prohibited by the Lorentz reciprocity theorem. However, it is possible to obtain interesting propagation direction-dependent properties by engineering the structure in order to exploit the non-Hermitianicity of the system. This was demonstrated in a taiji microresonator. As shown in Fig, 6 this device consists of a microresonator with an embedded S-shaped waveguide. Although the transmission in the two directions of excitation is the same, the reflection can assume completely different behaviors. When the light is counterclockwise coupled to the taiji microresonator (*forward* excitation), the system behaves as a typical resonator. Therefore, neglecting the Fabry-Pérot oscillations, the signal circulates into the external rim and the S-shaped branch is just a source of losses. The reflection is equal to zero and the transmission reassembles the common Lorentzian shape. On the other hand, when the light is clockwise-coupled to the taiji microresonator (*reverse* excitation), the S waveguide reverses the propagation direction. Hence, both the clockwise and the counterclockwise modes circulate within the external rim and the reflection is no more zero.

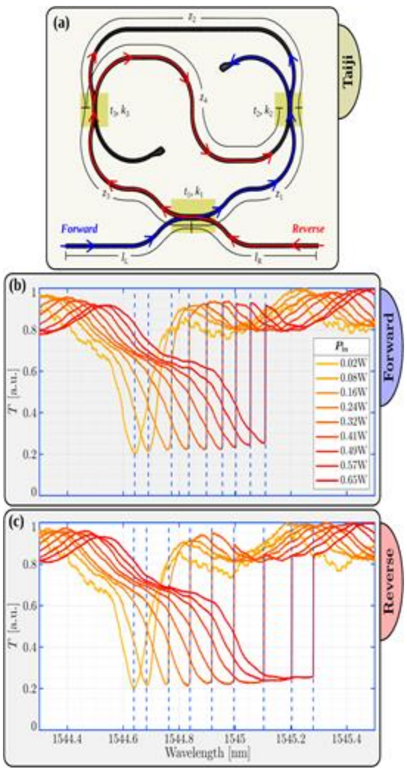

Figure 6: *Panel (a) shows the sketch of the taiji microresonator/bus waveguide system. The blue (red) arrows highlight the path followed by the light in the forward (reverse) configurations. Panels (b) and (c) display the experimental transmission spectra for an upwards wavelength ramp as a function of the input power for the forward and reverse orientations.*

The non-Hermitianicity of this system can be combined with the material nonlinearities in order to break the Lorentz reciprocity theorem. We have demonstrated a direction-dependent transmission in the nonlinear regime. Figure 6 (b)-(c) shows the experimental transmittance as a function of the incident wavelength for different input powers. Specifically, panel (b) and (c) display the *forward* and *reverse* excitation, respectively. The blue dashed lines highlight the resonant wavelengths for the different input powers. At low input fields, both excitations show the same Lorentzian shape and the resonant wavelength is denoted by the minimum of the transmittance. Increasing the input field, the transmittance goes towards longer wavelengths due to the internal energy of the taiji microresonator because of the nonlinear refractive index. This shift is characterized by a threshold where the transmittance jumps back to a value close to one. Therefore, the response reassembles a triangular shape. Higher stored energy gives rise to larger resonance shifts before the jump. Comparing panel (b) with panel (c), at sufficiently high power, the *reverse* excitation shows always a threshold wavelength higher than the *forward* one. This behavior is strictly connected to the asymmetry of the system. In fact, in the *forward* excitation, the light is partially lost at the ends of the S-shaped waveguide. On the contrary, in the *reverse* one, the S-shaped branch couples light from clockwise to counterclockwise mode increasing the stored energy.
In conclusion, a simple structure consisting of a microresonator with an embedded S-shaped waveguide behaves as a unidirectional reflector in the linear regime. Moreover, it allows breaking the Lorentz reciprocity theorem combining its non-Hermitian dynamics and the nonlinearity of the material. The direction dependence of the transmittance results in a different resonance shift in the *forward* and *reverse* excitation.

4. Multi-Source Hybrid ODE Solver Toolkit (Davide Bazzanella)

Photonics Integrated Circuits (PICs) contains increasingly complex structures. Both the design and the experimental investigation of these structures require a solid understanding of the phenomena involved, which translates in a (numerical) model able to predict experimental results. Moreover, there is a strong interest in studying the PICs response in the nonlinear regime. Different effects might induce nonlinear response, e.g. the Kerr effect, the two-photon absorption (TPA), the Free Carrier Dispersion (FCD), the Free Carrier Absorption (FCA), and the Thermo-optical (TO) effect. These nonlinearities are present even in the response of a single ring resonator and produce behaviors such as self-pulsing, bistability, and optical limiting. Figure 7 shows an example of a linear spectrum of a ring resonator and an example of nonlinear response of the same ring.
For these reasons, we developed a toolkit that allows the modeling of any complex structure and obtains its response both in the linear and in the nonlinear regimes.
The toolkit provides the following properties:

- a wide set of functions to define fundamental blocks such as an isolated waveguide or a ring resonator, which can be expanded to cover the needs of the user. These functions can be combined modularly to define complex PICs.
- a symbolic system that solves the problem of the linear propagation of optical fields within the structure and provides the user with a parametric function that evaluates such fields in all the structure.
- a model for evaluating the PIC temporal response to a given input, while taking in consideration the nonlinear optical effects. Several different response signals can be evaluated at the same time, by exploiting parallel computing toolboxes.
- a variety of tools and functions that allow to evaluate, store, retrieve, re-evaluate, analyze, and display the results.

This toolkit has been used to investigate the unexpected behavior of a single microring resonator and to help the design of novel structures in the PELM Project.

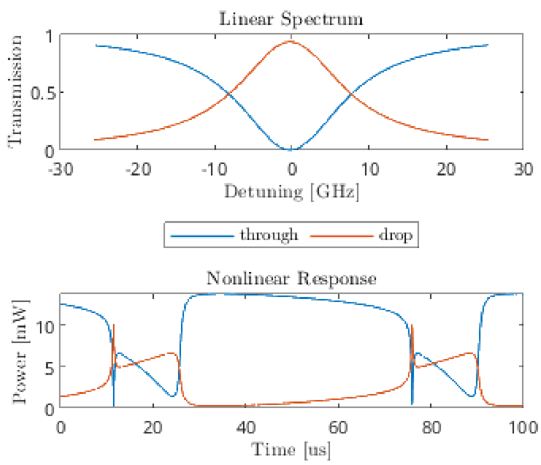

Figure 7: *examples of linear spectrum and nonlinear response of a ring resonator.*

5. Improved dynamical equations for the modelling of thermal and free carrier nonlinearities in silicon microring resonators (Massimo Borghi)

A well-known issue in silicon nanophotonic devices operating at telecom wavelengths is Two Photon Absorption. High quality factor silicon microresonators can easily reach circulating power intensities up to hundreds of MW/cm^2, triggering multiphoton absorption. As a side effect, free carriers are generated, whose relaxation self-heats the resonator and modifies its temperature. All the above-mentioned mechanisms increase the loss and modify the resonance wavelength of the resonator, compromising their operation as filters, delay lines, frequency converters or sources of squeezed light.

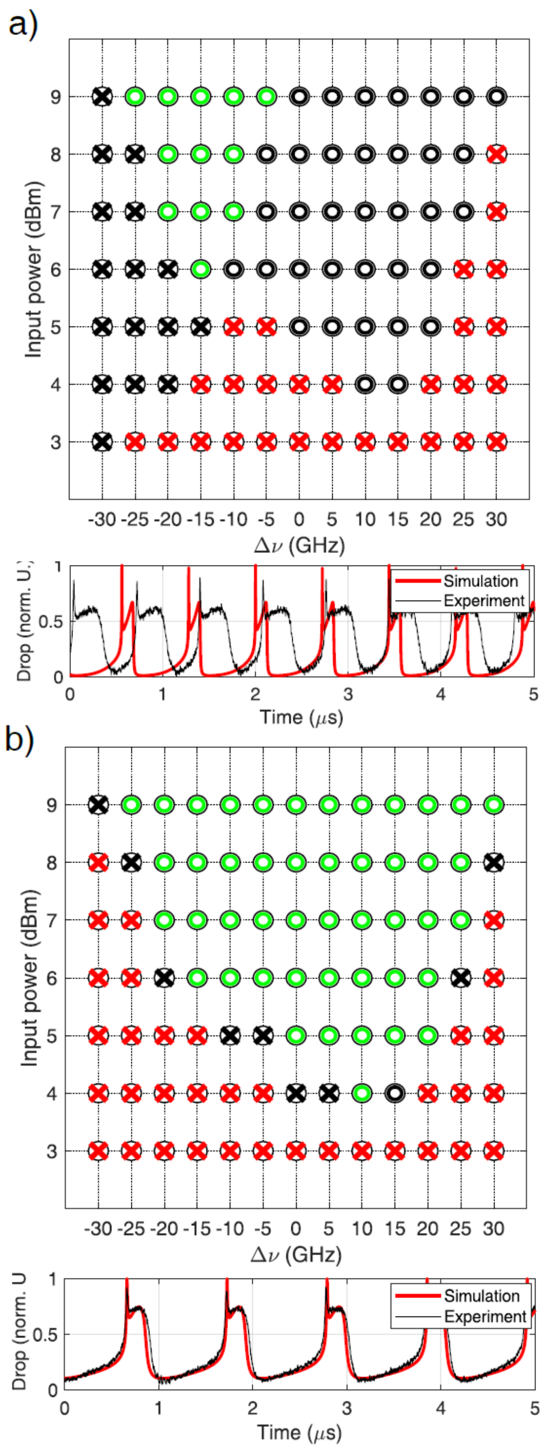

Figure 8. *a) Top: experimental stability map of the resonator as a function of the input power and the detuning of the laser frequency with respect to resonance. Crosses label stable states, while circles identify a self-pulsing (SP) regime. When the simulation fails to predict the same type of stability observed in the experiment, the corresponding label is shown in black. Bottom: example of temporal waveform (black) at the output of the resonator, and corresponding trace (red) predicted by simulation. Both panels use Newton's law of cooling for the temperature equation [3]. (b) Same as (a), but adopting our refined temperature equation.*

Moreover, the simultaneous action of thermal and free carrier dispersion can drive the resonator into a self-pulsing regime, where the light intensity periodically varies in time even if the input excitation is continuous wave (CW). The development of a theoretical model that describes these combined effects is then relevant for every field of integrated photonics that relies on resonant structures. In our work, we refined the coupled equations describing the dynamics of silicon microresonators under thermal and free carrier nonlinearities. We show that, for resonators buried in a silicon dioxide cladding, the Newton's law of cooling, which was traditionally used to model its temperature behaviour, can be inadequate. In these cases, numerical simulations predict stability regions, light temporal waveforms and drifts of the resonance frequency that deviate from the experimental observation. An example is shown in the top panel of Fig. 8(a), where we experimentally probed the dynamical state of a resonator in the parameter space spanned by the input pump power and the detuning of the laser frequency from resonance. The classification is based on whether the resonator is found in a self pulsing or stable regime. Very few experimental points match the dynamical state predicted by simulation. Here, we use the standard set of coupled ordinary differential equations (ODE) for describing the light intensity, the temperature and the free carrier population. The temporal waveforms at the output of the resonator also disagree with the simulations, as shown in the bottom panel of Fig. 8(a). We found that the origin of this discrepancy lies in the temperature equation, which derives from Newton's law of cooling. Through Finite Element Method (FEM) simulations, we identified that Newton's law lacks of an inertial term that is responsible for a slower thermal decay rate of the resonator. A new differential equation, that we train to reproduce the FEM simulation, is introduced to fix the discrepancies with the experimental results. As shown in Fig. 8(b), the new model correctly predicts the stability regions of the resonator (less than 20% of unmatched classifications), and simultaneously improves the agreement with the experimental temporal waveforms. We also explored the range of applicability of our model, and the cases where Newton's law provide, nevertheless, an accurate description of the ring behaviour. This work completes the comprehension of thermal and carrier dynamics in silicon resonators, and can be especially helpful for the design and performance assessment of telecommunication devices or dynamical nodes for neuromorphic computing.

6. Experimental demonstration of reservoir computing with a silicon resonator and time multiplexing (Massimo Borghi, Stefano Biasi)

Reservoir computing (RC) is a machine learning paradigm where a recurrent nonlinear dynamical system is used to process information from the input to the output layer of a neural network. This replaces the multiple hidden layers used in deep learning. Only the weights of the output layer are trained, typically using linear regression techniques. Photonic hardware has been implemented to build reservoirs with very high operational speed, demonstrating state of the art performances for a large variety of tasks. Beside, reducing the hardware dimension, the dense integration of optical components on a photonic chip simplifies its control and management and improves the power consumption. However, the experimental demonstrations of RC with integrated optics are still very limited. Most focus on spatially distributed nodes, which are interconnected by delay lines and splitters, but the loss of the components and the inherent topology of the interconnections make them difficult to scale. We propose and validate an RC architecture based on a single dynamical node, a microring resonator and time multiplexing. The concept is shown in Fig. 9(a). We encode the input (analog or digital) information in the intensity of a pump beam, which is serially injected into the microring resonator. Here, it is transferred to the free carrier concentration by Two Photon Absorption (TPA). By adopting a time scale close to the free carrier lifetime, the resonator is constantly kept in transient dynamical state. A secondary probe beam, tuned on an adjacent resonant order, tracks the resonance shifts induced by free carrier dispersion, which imprints variations on the output light intensity (Fig.9 (a)). Multiple points are sampled at specific times, synchronously with the rate of injection of input samples. These represent the virtual nodes at the output layer of the reservoir. The required nonlinear transformation among layers is provided by TPA and by the complex relationship between the transmitted intensity and the instantaneous free carrier population. The connectivity among virtual nodes is ensured by the inertial response of the free carriers to changes of the input pump power, which induce a fading memory. The type of interconnection topology which establishes is that of a linear chain. We used regularized Ridge regression to train the set of weights associated to the virtual nodes at the output to classify specific patterns presented at the input. Two nontrivial tasks are tested: the delayed XOR (digital encoding) and the classification of Iris flowers (analog encoding), for which we achieved a highly competitive value of accuracy of $(99.3 \pm 0.2)\%$ at MHz rates. As shown in Fig.9 (b), the reservoir has a classification error, which depends on the input power, with a clear optimum. This marks the transition from a rich dynamics governed by thermal and free carrier effects, where the reservoir shows its maximum separability, to an irregular one, in which the microring self-pulses. This statement is supported by numerical simulations, which validate our recently developed model. Starting from this building block, we discussed several strategies to realize spatio-temporal reservoirs of increased complexity, hosting thousands of virtual nodes and operating at GHz rates. These proposals all leverage on the silicon photonics platform, hence they are compact, low power consumption and mass manufacturable.

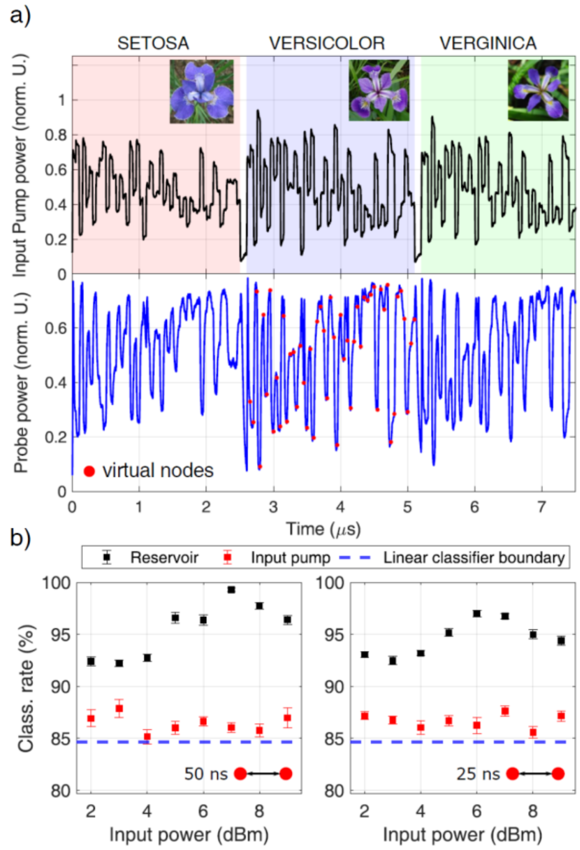

Figure 9: *(a) Example of waveform of the input pump (top panel, in black) and of the probe at the output of the resonator (bottom panel, in blue) for 50 virtual nodes injected at bitrate of 20 Mbps. Different background colours highlight the subspecies of the Iris flower to be classified. A representative picture of them is shown in the insets of the top panel. Virtual nodes sampled from the probe trace are indicated by the red dots in the central band. (b) Iris flower classification rate as a function of the average input power for bitrates of 20 Mbps (left) and 40 Mbps (right). Black scatters use virtual nodes sampled from the output probe while red scatters from the input pump. The dashed blue line is the lower bound in the classification rate obtained by feeding the input samples into a linear classifier, without electro-optic conversion.*

7. SCISSOR as a Neural Network (Dhouha Jemmeli, Stefano Biasi)

The way in which information is elaborated inside neural networks seems to be more favorable, in comparison to the Boolean logic, to the development of photonic integrated processors. The aim of photonics is to overcome the performances of electronics in the development of neuromorphic networks by exploiting its inherent suitability to parallel computing, its bandwidth and speed, and its power efficiency. Many neuromorphic networks are based on the Reservoir Computing (RC) approach, which is a learning method that allows having little to no control on most of the network while employing all efforts on the training of a single output layer. In this work, a reservoir implementation is designed and numerically simulated by considering silicon integrated microring optical resonators as nonlinear nodes.

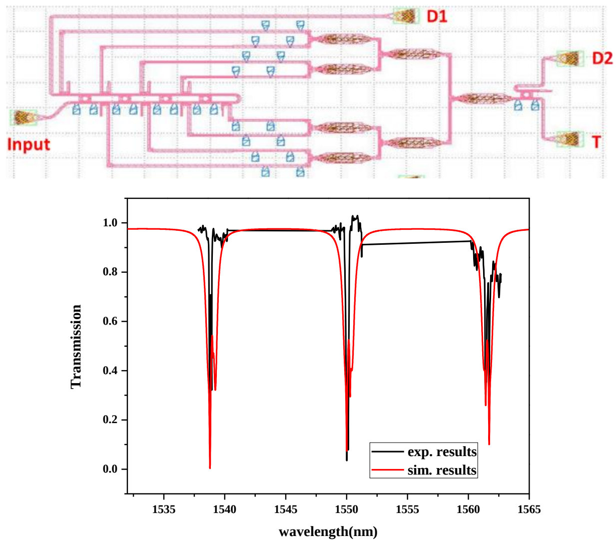

Figure 10: *4 resonators SCISSOR with complex readout perceptron. Blue tracks are the electrical controls for the thermal tuning. Transmission spectra of the SCISSOR, experimental data with black color, fit with red color.*

The analysis of the single micro-resonator enables us to study in a better way the SCISSOR geometry. By sequentially coupling ring resonators to a waveguide with a fixed spacing (Fig. 10), one has a SCISSOR that behaves as the reservoir in the RC network. In our case, we use a SCISSOR with 4 ring resonators. The reservoir internal states are sampled in eight different points by using directional couplers along the bent waveguide. Then, we perform the complex sum of these 8 signals (phases and amplitudes). Finally, we couple the resulting field to a single micro-resonator that plays the role of the nonlinear activation function. The resonance wavelength of the output microresonator can be thermally tuned. Therefore, the network is made by a SCISSOR as the reservoir and a complex perceptron in the output. As a first step, we measured the spectral response of the SCISSOR (Fig. 10) at the D1 port. We simulate the response of the SCISSOR by using the transfer matrix method (TMM). By comparing the experimental and simulated transmission spectra of the SCISSOR (Fig. 10) we observe an agreement and no transmission peaks. This is explained by the interference between the fields dropped by the rings and the fields going through the rings and coupled back by the bent waveguide.

8. All-optical complex perceptron for ultrafast data processing (Mattia Mancinelli, Davide Bazzanella)

The first chip fabricated within the BACKUP Project contains several different structures belonging to the two separate approaches of feed forward neural networks (NN) and reservoir computing (RC). Among the many structures, we focused on the so-called complex-valued perceptron (CP), which is a passive all-optical feed forward NN. Our implementation has been developed to work with sequences of bits: the input (optical) signal is divided in four signals, which are then delayed and a constant phase is added to each one of them. In our case the four signals have a fixed delay of $\Delta T_j = j\ \Delta T$ while the (complex) phases can be adjusted in the range 0-2π. The resulting signals are then four copies of the input signal, each one with a different delay and a different phase. The last part of the NN combines these four signals into the single output (optical) sequence. After the optical summation, a photodetector provides the necessary nonlinear activation function that allows the network to work as it is. Figure 11 shows a simplified schematic of the network.

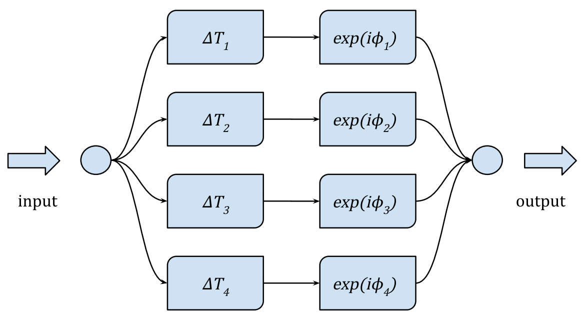

Figure 11: *simplified schematic of the complex-valued perceptron network.*

The output of the network should correctly represent the result of a digital operation, a task, on the input bits. However, the initial values of the four phases are not necessarily the best ones to carry out this task, so we need to modify the network response by changing the value of the phases. To modify our network response to get the target result – ie. to train the network – we use the particle swarm (PS) algorithm, a gradient-free optimization algorithm. We ask the PS to find the optimal values for each of the four phases so that the output signal gives the most correct results. So far, we have studied two tasks: the pattern recognition and the delayed XOR operation. The first one, is a linearly separable problem, which analyses sequences of n-bits and produces a high output when a specified sequence is found, a low output otherwise. The second one is a nonlinearly separable problem, in which the logical operation XOR is applied to two bits separated by a certain delay. The XOR operation produces a high output when only one of the two bits is high, a low output otherwise. Figure 12 shows the optical input and output signals as well as the target sequence for the XOR task. As we can see, the output (red) correctly predicts the target (green), obtained carrying out the task on the input (blue).

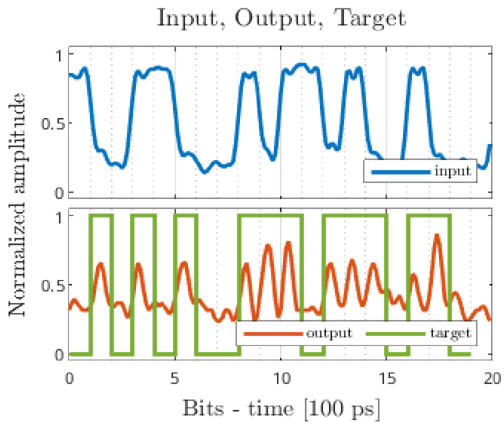

Figure 12: *(top panel) input optical signal. (bottom panel) output optical signal, target sequence.*

In the next future we will investigate the effect of the optical nonlinearities provided by microring resonators, such as the Kerr effect, the two-photon absorption (TPA), the Free Carrier Dispersion (FCD), the Free Carrier Absorption (FCA), and the Thermo-optical effect (TOE). We expect that by adding these nonlinearities and tuning them properly the complex perceptron will perform better than without.

9. Modelling of Nonlinear ring dynamics for Reservoir Computing (Mattia Mancinelli)

Reservoir computing (RC), a computational paradigm inspired on neural systems, has become increasingly popular in recent years for solving a variety of complex recognition and classification problems. Thus far, most implementations have been software-based, limiting their speed and power efficiency. Here, we present the modelling of an all-optical reservoir network based on a microring (MR) resonator, a delay line stage and a complex perceptron (CP). The CP is the complex valued implementation of the widely used linear classifier. The system under study is reported in Fig. 13.

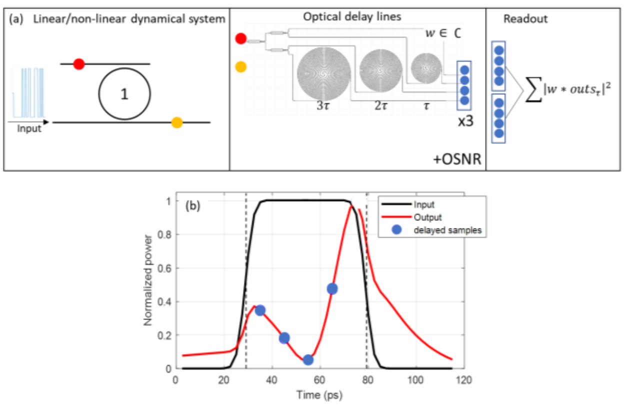

Figure 13: *(a) RC network composed by a micro-ring resonator, all-optical delay lines and the readout stage. (b) Binary optical input (black), microring drop port output (red) and delayed samples created by the optical delay line stage (blue circle)*

The microring linear/non-linear dynamics mixes the information present in the input modulated signal that is then extracted by the delay line stage. The type of dynamics is dictated mostly by the input power. Above a certain threshold, two photon absorption and free carrier (FC) effects are triggered. The delay line stage, used after the through (orange) and drop (red) ports, exploits the memory added by the MR as inter-symbolic interference by observing, at different times, how the bit is changed. Consequently, N delayed samples per port are created (blue circles) that are then weighted and summed in the complex domain in the readout stage. The detection applies the non-linear transformation $|\cdot|^2$. The device training is performed at the readout stage where a set of complex weights are chosen to minimize the error done by the network in performing a particular task.

We analyse the network performance using a binary modulated input at 10Gbit/s, 4 delay lines (N=4) at several input powers and free-carriers timescale on the delayed XOR task. In this task, the network has to produce an output that corresponds to the XOR applied to two consecutive bits in time: $XOR(bit_i, bit_{i-1})$, where i is the bit counter. White noise is also added at the input to test the network robustness at different Optical SNR. The resonance-input detuning is fixed at 15 GHz to maximize the system non-linearity. The results are shown in Fig 14.

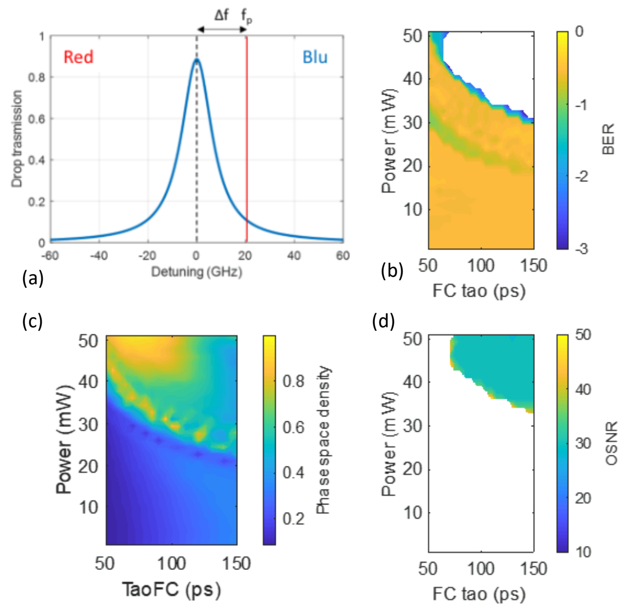

Figure 14: *(a) Microring drop transfer function in linear regime where the input frequency is shown in red. (b) BER as a function of input power and FC tao. Void area identifies error free operation. (c) Phase space density map. (d) OSNR required for error free operation.*

The scan on the input power allows highlighting whether linear or non-linear dynamics promotes the task solution, while the scan on the FC tao (free carrier lifetime) helps in matching the non-linearity timescale with the input bitrate. Complex dynamics in the reservoir are associated with a dense phase space. Phase space density map is reported in Fig. 14(c). Rich dynamics helps the reservoir simplifying the task before the classifier. Panels (b) and (d) report as a function of input power and FC tao: the network BER and the OSNR required for the error free operation (BER = 0). There is a clear correspondence between the dense phase space area and low BER. Here, the network is in a non-linear regime and requires a FC lifetime lower than the bit width (100 ps).

10. Delayed network based on a single microring resonator (Giovanni Donati)

In the context of delay-based reservoir computing, the system schematized in Fig. 15 has been numerically investigated and tested on time-series prediction tasks.

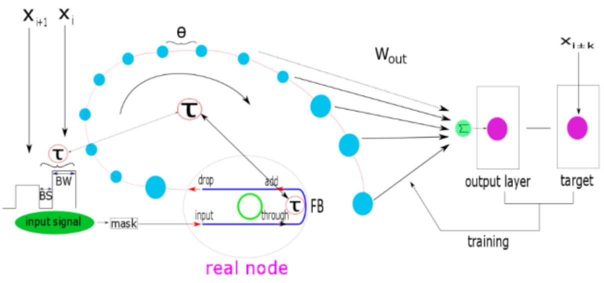

Figure 15: *scheme of a delayed-based reservoir computing using as a real node a silicon microring resonator. The name delayed is used to specify the presence of a feedback (FB), which depending on its length can be integrated in the chip or realized via optical fiber.*

Each input series element is translated in an optical pulse of duration BW, according to a sample and hold procedure, then masked and sent to the input waveguide of a ring in add-drop filter configuration, the nonlinear real node. The drop output signal is sampled at different time and accommodates the values of the nodes composing the reservoir. A feedback line reintroduces in the add port of the system a delayed version of the through signal. Its length depends on the delay time (τ) one is looking for, which is synchronized with the time of the input sample and hold operation and virtual node sampling. The choice of this parameter, between many others in the model of the system, and the shape of the input series itself affect how the free carrier and thermal nonlinearities contribute to the dynamic of the ring. An example where free carrier nonlinearities are the predominant is shown in Fig. 16 during a SantaFe time-series prediction.
Configurations where also thermal contribution is important can be achieved when the time interval between optical input peaks matches the thermal timescales. This task turns out to be solved also without feedback and indicates that nonlinearities provide a source of sufficient nonlinear memory. Anyway, this is not generally occurring for other prediction tasks which rely also on memory provided by the feedback. A better clarification of this last point is actually the subject of my study.

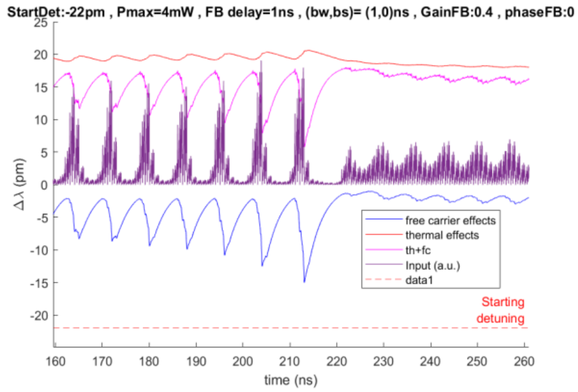

Figure 16: *Example of SantaFe prediction task solved exploiting free carrier nonlinearities. The larger thermal timescale makes the temperature unable to follow the faster input, ending up in a small contribution to the resonance shift.*

This work is carried out within a joint co-tutelle agreement with the University of the Balearic Islands (Spain).

11. A FEM enhanced Transfer Matrix method for optical grating design (Clara Zaccaria, Mattia Mancinelli)

We implemented and generalized a new method for grating design in integrated photonics. In literature there are a plenty of solutions found in order to optimize grating efficiency, which involve mainly grating geometry: periodic grating, aperiodic gratings, apodized gratings, double etched gratings.

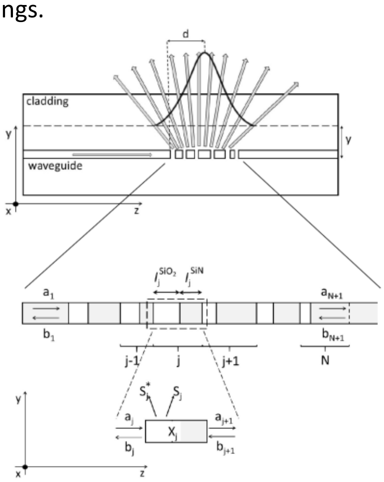

Figure 17: *Sketch of the system: the grating is composed by blocks with the SiO_2 and SiN sections*.

Our method will focalize on the design and geometrical optimization of aperiodic grating. We propose a method based on the transfer matrix formalism enhanced by a physical simulator. In this way, we get the physical insights typical of simulator-based methods and the speed of machine learning approaches. The goal of the method is to find the optimum layer sequence of a grating in order to obtain a desired distribution of the scattered field. Taking for example a SiN waveguide embedded in a SiO_2 cladding, we model the grating as divided in blocks, each one formed by a SiO_2 section and a SiN section. Each block is characterized by different lengths of the two sections as shown in Fig. 17. The proposed method is based on the following assumptions:

1) each single block acts as a scatterer and the scattering depends only on the SiO_2 section;
2) the individual blocks are independent i.e. the presence of one block does not influence the behaviour of the others;
3) the propagating field is a waveguide propagation mode;
4) propagation losses in the grating are neglected;
5) the scattering profile the single block is calculated only once with a FEM simulator for all the different SiO2 layer lengths;
6) The reflection and transmission coefficients of each SiO2 layers are calculated only once by a FEM simulation for all the different SiO_2 layer lengths.

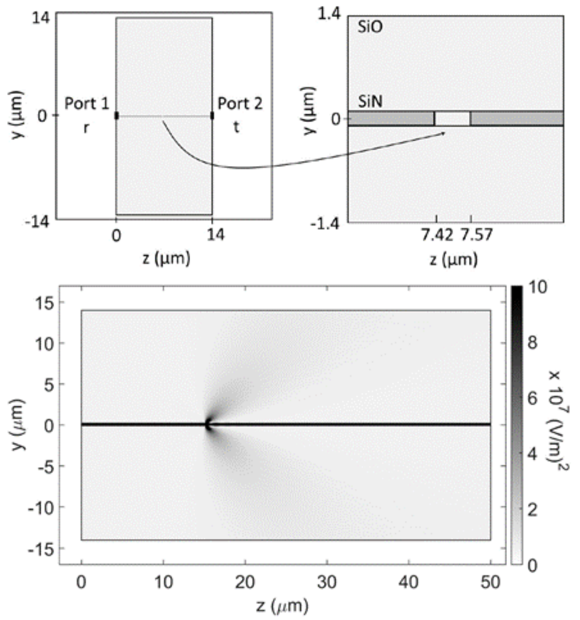

Figure 18: *(top) FEM simulation domain to compute the single block parameters where a single SiO_2 layer is interposed in a SiN waveguide cladded by SiO_2. Here the SiN waveguide is 150 nm high and the SiO_2 layer is 250 nm long. The two thick vertical lines (not in scale) show the positions where the fields are computed to extract the rj (Port 1) and tj (Port 2) parameters. (bottom) Scattering map for a forward propagating optical mode. The dark horizontal line refers to the optical mode which propagates in the waveguide. The gray scale refers to the field intensity and is given on the right of the panel. The simulation is done for a 488 nm wavelength and with the parameters shown in the top panel, a part a longer waveguide.*

The overall scattered intensity by the grating is then computed as the overlap of the fields scattered by each block (Fig. 18). Validation of the method with respect to a full FEM simulation shows no differences in the scattered profile. Once defined the target-scattered profile that should be generated by the grating, an optimization algorithm (the particle swarm algorithm) is used to choose the optimal grating geometry (i.e. SiN and SiO_2 lengths). The method has been validated on many different cases and we found that the computational time required to optimize a grating is significantly reduced with respect to a full FEM simulator (hours with respect to days).

12. Packaging of a chip designed for localized neuron excitation (Clara Zaccaria, Beatrice Vignoli)

One of the goals in BACKUP project is the creation of a hybrid platform in which a photonic chip and a neuronal culture compute together. As a first step of this project, we want to be able to grow neurons on the surface of a photonic chip and to excite them with the light coming from the chip, taking advantage of optogenetics. To this end, we designed a chip where waveguides terminate with diffractive gratings (hereafter named *scatterers*), in such a way that a spot with the diameter of about 10 µm is formed on the surface of the chip. The chip, shown in Fig. 19 presents two different parts: part A has single inputs which lead to test structures and arrays of scatterers after a combination of multi-mode interferometers (MMIs), while part B has single inputs that address the light to single scatterers, arranged in a 4x8 matrix. All the optical structures were tested: the grating scatterers have an efficiency of 45% and the more lossy combination of optical structures gives a total loss of -16 dB.

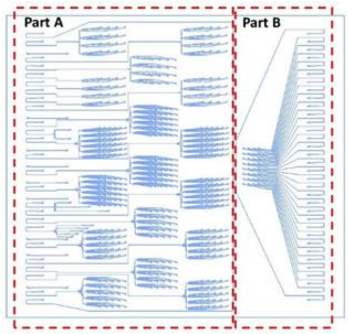

Figure 19: *Sketch of the designed chip.*

The inputs consist in grating couplers. To insert the light signal we used 34-fibers fiber arrays. In order to align the fiber array to the chip, a custom alignment stage was implemented: a teflon tweezer holds the fiber array and the system is carefully moved thanks to a 3-axis stage. The chip is glued to a glass substrate and the fiber array is moved in order to be aligned in the proper position. Once the fiber array is aligned to the inputs of the chip, everything is glued in position (Fig. 20).

Subsequently, the glass substrate with the chip and the fiber array is put inside a dish with a small window from which fibers can come out. The window is then sealed with silicon. The whole system can be positioned under the microscope (Fig. 21) in order to perform experiments with neurons. Once neurons are plated inside the dish, light coming from the chip will be able to excite the optogenetically transfected neurons lying on its surface.

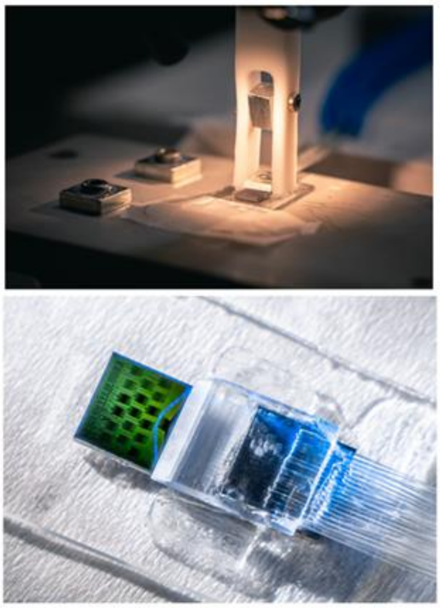

Figure 20: *In the upper photo is shown the alignment system; in the bottom part is shown the fiber array aligned to the chip and fixed with glue. Note the thin blue line on the chip surface, which demonstrates the ability to inject blue light into the chip by the aligned fiber array.*

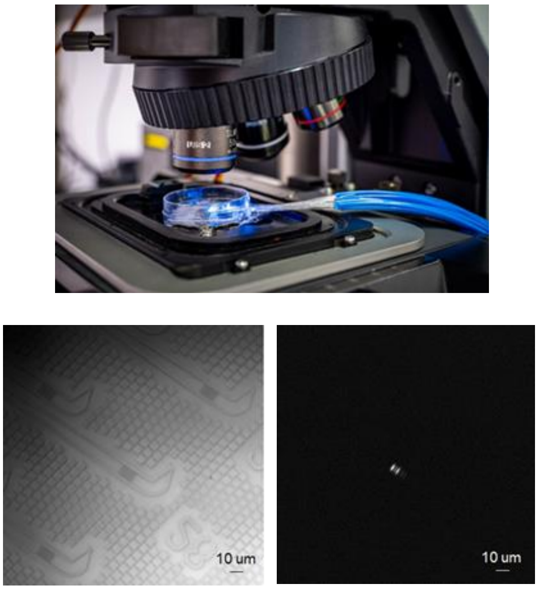

Figure 21: *On the upper part is shown the composed system under the microscope. In the bottom part, on the left is shown one of the scatterers seen from a 20x objective; on the right is shown the generated light spot.*

13. Astrocytes and engrams (Beatrice Vignoli)

Understanding how memories are formed and maintained in the brain remains one of the most attractive goals of neuroscience. Memories are believed to be stored as permanent changes (“engram”) involving a reinforcement of synaptic connections among specific neurons. To be created, memories must be converted from an initially state in which they are susceptible to deterioration, into stable forms, a process called “memory consolidation". The mechanisms for this conversion go from long-lasting molecular adaptation at synaptic level, to refinement of the whole neuronal network. Recently, we demonstrated that also astrocytes, a non-neuronal component of synaptic contacts, could provide local support in the strength of neuronal connections playing a crucial role in memory consolidation.

Astrocytes are not electrically excitable cells and express spontaneous calcium transients at perisynaptic contacts, suggesting for a self-governing action in synaptic functions. These calcium transients mediate the release of neuroactive substances called gliotransmitters. Once released, these molecules could bind to postsynaptic receptors, regulating neuronal excitability, a mechanism required for memory consolidation. Thus, spontaneously active astrocytes acquire molecular control of synaptic stabilization and memory retention upon initial neuronal instruction. This process spreads memory engram information over perisynaptic astrocytes in addition to pre/post- synaptic neurons, creating two networks that interact each other to stabilize and preserve memories following initial neuronal instructions.

The molecular machinery governing memory consolidation employs complex biochemical processes that can play at different time scales. We are now attempting to understand how these processes are orchestrated to maintain memories over a lifetime. To interpret the complex organization of the molecular interactions among neurons and astrocytes at synaptic levels we will generate computational models to abstract neuron- astrocytes interaction in memory consolidation.

14. Measurements of electrophysiological activity in neuronal cultures using microelectrode array (MEA) (Ilya Auslender, Beatrice Vignoli)

Electrophysiological activity of neurons is measured to study the functionality of the culture. These measurements can be used as a technique for reading the induced memories (engrams) in the neuronal network. The measurement is performed by sampling and recording electrical signals from neurons cultured (in-vitro) on microelectrode array (MEA). Typical MEA configuration is shown in Figure 22. The electrical signals are filtered and amplified by an electronic system, recorded in a computer where further analysis can be performed. In our setup, we use a MEA-2100mini System (Multichannel systems GmbH). The array chips, which were used in experiments, have a configuration of 60 electrodes (8×8 grid without the corners) of 10 µm diameter and 100 µm spacing. Another chip with 30µm diameter electrodes, 200 µm spaced apart, was also used.

The basal electrical signal consists mostly of thermal noise. After the neurons are plated on the MEA chip, additional biological noise may be present.

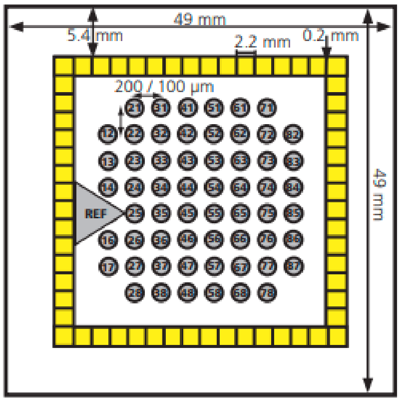

Figure 22: *Sketch of a typical MEA chip*

An illustration of recording of raw signals from each electrode of the MEA is presented in Fig. 23. The signals extracted from the recording are the action potentials, which indicate an activation of a single neuron or of group of neurons within the network. These signals are commonly known as "spikes". To extract the spikes from the noise, first the signal should be bandpass filtered to a specific frequency band where common spikes are present. A spike threshold detection algorithm is then applied on the filtered signal. Here, a spike is detected when the potential exceeds a threshold value (usually negative voltage), which is few times larger than the characteristic noise signal. In Figure 24, an example of a recording from MEA is shown, where spike detection is applied.

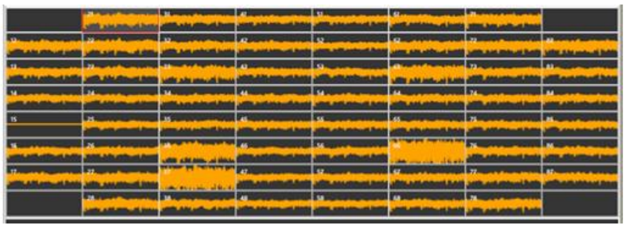

Figure 23: *Raw data recorded from MEA*

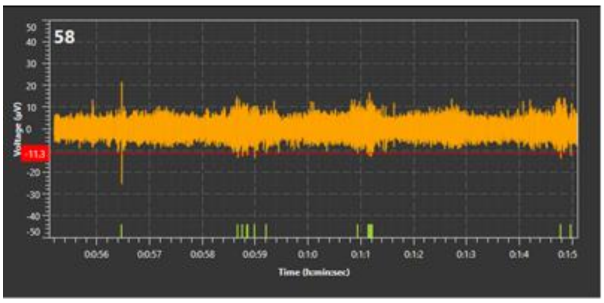

Figure 24: *Spike detections from filtered MEA data*

The raw data is then further analyzed to obtain a detailed map of the culture activity. The map is compared with a microscope image of the neuronal culture (Figure 25) to understand which of the neurons were activated. This allow characterizing a specific circuit in the network and, by that, "reading a memory" from the culture.

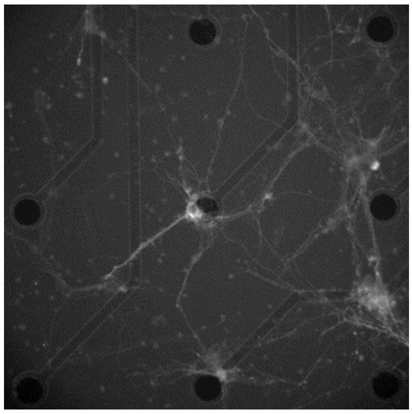

Figure 25: *Image of ChR2 transfected neurons on a MEA chip (a partial close up of the chip). Distance between electrodes = 100μm.*

As a first step, we analyzed our cultures by their spontaneous activity, i.e., measuring spontaneous spikes (without stimulation). Our goal was to track the activity of the culture each day in-vitro (DIV). The activity of the culture was characterized by its mean firing rate (MFR), i.e., the number of spikes per time of recording (Fig. 26).

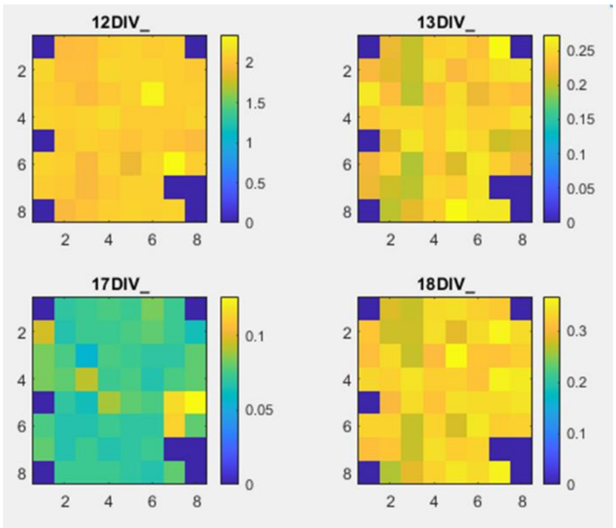

Figure 26: *Tracking of the spontaneous activity of a neuronal culture in terms of mean firing rate (MFR). The color bar indicates number of spikes per second.*

In a next step, we plan to perform MEA recordings following optical stimulation executed by digital light processor (DLP). Using DLP, we create stimulation patterns (both temporal and spatial) in order to induce engrams in the culture ("write memory") and by using MEA we will record the electrophysiological response of the neurons to observe the created synaptic connections between specific neurons and to extract the circuity of the network ("read memory").

15. Near-ideal spontaneous photon sources in silicon quantum photonics (Massimo Borghi, Stefano Signorini)

Recent quantum optical experiments demonstrated that classical computers can be surpassed by quantum architectures in solving highly specialized problems. However, general purpose quantum computers require millions of components to run their architecture, becoming quickly unfeasible with bulk optics technologies. The most promising approach to scalable quantum computing architectures is silicon photonics. The efficient use of quantum resources is determined by the quality of the single photons. They have to be pure, indistinguishable and available in a large number on chip. However, current single photon sources cannot satisfy all these conditions simultaneously. In our work, we demonstrate the first integrated source able to meet all these requirements: high purity, high indistinguishability and high heralding efficiency.

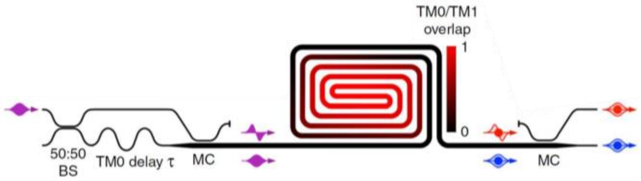

Figure 27: *A sketch of the source design. The pump, signal and idler pulses are represented in purple, red and blue respectively. The pump is split by a beam splitter (BS), delayed by τ and converted to the TM1 via a mode converter (MC).*

We developed a heralded single photon source based on intermodal spontaneous four wave mixing (SFWM) in multimode Silicon-On-Insulator waveguides. We used transverse magnetic (TM) polarization, exciting the pump on both the fundamental (TM0) and first order (TM1) modes, as sketched in Fig. 27.

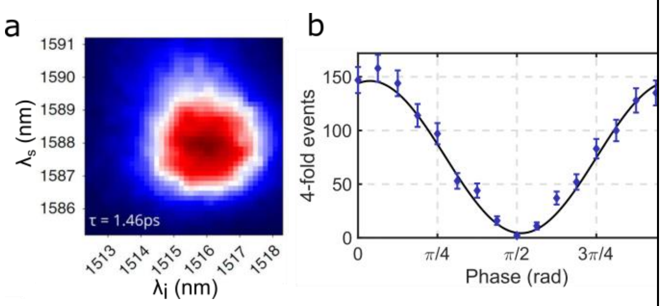

Figure 28. *a) Measured JSI of the source. b) Measured heralded HOM fringe between photons heralded from distinct sources. The phase controls the reflectivity of the beam splitter where they are interfered, with $\pi/2$ corresponding to a splitting ratio of 50/50 while $[0, \pi]$ to 100/0 and 0/100 respectively.*

By applying the proper delay to the faster TM0 mode, we made the two pump pulses to overlap only in the middle of the multimode spiral waveguide. This results in an adiabatic switching of the nonlinear interaction, unlocking near-unit spectral purity. The idler and signal photons are generated in discrete bands at 1516 nm on the TM0 and at 1588 nm on the TM1 modes respectively. By measuring the Joint Spectral Intensity (JSI), in Fig. 28a, we demonstrated that our source produces heralded single photons with a purity of 99.04(6) % while keeping an on-chip intrinsic heralding efficiency of 91(9) %. Via a reversed Hong-Ou-Mandel (HOM) experiment, we measured an indistinguishability between two sources of 98.7(2) %. As a last step, we demonstrated a record heralded HOM visibility of 96(2) %, shown in Fig. 28b. These results set a new benchmark for on-chip single photon generation, paving the way to large scale and fully integrated photonic quantum information architectures.

This work has been carried out in collaboration with Dr. Stefano Paesani, Mr. Alexandre Maïnos and Prof. Anthony Laing from the University of Bristol.

16. A source of mid infrared heralded single photons in silicon photonics (Matteo Sanna, Stefano Signorini)

The quantum properties of light are of high interest for sensing and metrology. Entangled and single photon states can be leveraged to overcome the limitations faced by classical technologies. By using single photon states, for example, the standard quantum limit (SQL) can be surpassed, increasing the accuracy of the measurement. Using entangled photons, it is possible to perform spectral sensing with improved performance at wavelengths that classically are difficult to explore. These quantum properties can be useful for gas sensing in the mid infrared (MIR), where gas absorption lines are typically orders of magnitude more intense than in the visible range. However, single photon generation and detection in the MIR is still not mature.

The aim of this work is to develop an on-chip single-photon source in the MIR. We used the generation of heralded single photons via intermodal spontaneous four wave mixing (SFWM). Given two photons at the same wavelength as input (at 1550 nm in our case), these are converted into two new photons at different wavelengths, the idler and the signal. Idler and signal are symmetrical in frequency with respect to the input photons and are time correlated. Being time correlated, the detection of the idler "heralds" the presence of the signal, whose detection is conditioned on the idler one. This heralding operation induces a single photon statistic on the signal beam, which is the actual single photon state produced by the source.

We designed and tested a heralded single MIR photon source on a single silicon integrated photonic circuit. The chip has been designed to generate the idler in the NIR (Near Infrared) and the signal in the MIR. To characterize the performance of the source and that its emission is truly at the single photon level, two parameters have to be measured: the coincidence to accidental ratio (CAR) and the heralded second order coherence function, indicated as heralded $g^{(2)}$.

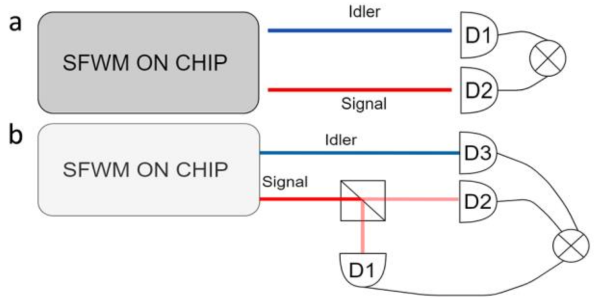

Figure 29. *(a) Sketch of the detection scheme for the signal-idler coincidence detection and (b) for the three-fold coincidence detection.*

The CAR has been measured by monitoring the signal-idler coincidences, as indicated in Fig. 29a. The higher the CAR, the higher the probability to detect a true coincidence over the noisy ones, the higher the reliability and brightness of the source. To evaluate the heralded $g^{(2)}$, the signal is split in two beams by a beam splitter, and their detection is conditioned by the idler detector, as shown in Fig. 29b. To demonstrate the single photon character of the source, a heralded $g^{(2)} < 0.5$ has to be measured. In Fig. 30a we report the measured CAR as a function of the input CW power. We achieved a maximum value of 145(8), the highest ever reported for an integrated source. In Fig. 30b the measured heralded $g^{(2)}$ at 41 mW is shown as an example. The minimum heralded $g^{(2)}$ value is 0.09(2), measured at 21 mW, demonstrating the single photon character of the source.

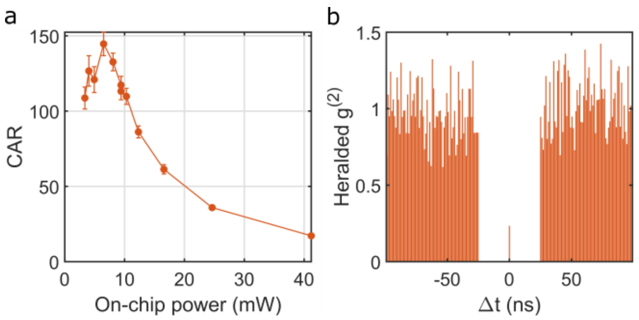

Figure 30. *a) CAR as a function of the on-chip pump power. b) Measured heralded g(2) at 21 mW of pump power.*

With these measurements we demonstrated that our heralded source can be operated with high efficiency at the single photon level in the MIR. The next step is to use this source to perform gas sensing in the MIR at the single photon level, thus exceeding the SQL of classical technologies.

17. Certified quantum random numbers using single - photon entanglement (SPE) from a laser source (Nicolò Leone, Stefano Azzini)

Entanglement is one of the most valuable resources offered by quantum mechanics: its applications are essentially endless. In quantum information, in particular, previous works have proposed and experimentally proved that entanglement is a witness of randomness. The latter is a fundamental characteristic when we consider cryptographic applications, where random numbers are employed to protect sensible information. The security of nowadays cryptographic protocols is based on the unpredictability of the random sequence used. However, the a-priori proof of the randomicity of a sequence generated exploiting classical processes cannot be guaranteed. Therefore, the sequence has to pass multiple and often demanding statistical tests in order to be accepted as random to a certain extent. The very nature of quantum mechanics makes it possible not only to generate intrinsically random numbers, but also to certify them. Indeed, by exploiting the non-classical correlations of entanglement, it is possible to give an upper bound to the level of knowledge of the generated sequence that an external eavesdropper can eventually achieve. The figure of merit in these situations is the min-entropy, which translates into an estimation of the effectiveness of the best strategy of guessing the generated sequence.

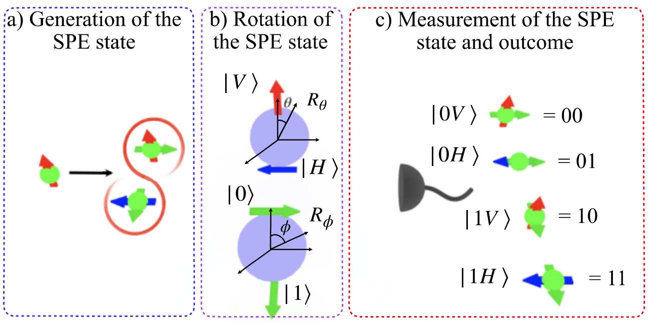

Figure 31: *Methodology of generation of the random numbers. a) First the SPE state is generated at the single photon level. b) The different degrees of freedom of the SPE state are rotated by two angles($\boldsymbol{\varphi}, \boldsymbol{\theta}$), which define the unitary operation $\boldsymbol{R_{\varphi}}$ and $\boldsymbol{R_{\theta}}$. These rotations are necessary to verify the presence of the non-classical correlations due to entanglement. c) The rotated state collapses in one of the possible four states that compose the Hilbert space (|0>, |1> stands for momentum and |V>, |H> for vertical and horizontal polarization) when a measurement is performed by using single photon detectors. The detected state, here in binary representation, identifies the bits that will constitute the random numbers of the generated sequence.*

Inspired by this possibility, we proposed a Quantum Random Number Generation, QRNG, protocol that allows estimating the min-entropy of a sequence of numbers represented by entangled single photons detection events (Fig. 31). Single photon entanglement yields non classical correlations between two degrees of freedom of a single photon, e.g. momentum (propagation direction) and polarization. Compared to inter-particle entanglement between two photons, the generation can only involve linear optical components, e.g. beam splitters and waveplates, and the detection does not require coincidence measurements. The protocol of generation of the random numbers is shown in Fig. 31: once generated the SPE state from an attenuated laser source (Fig. 31a), the degrees of freedom that compose the latter are rotated performing unitary transformations R_φ and R_θ (Fig. 31b). The random numbers are then obtained by observing the outcomes of successive measurements operations on SPE states (Fig. 31c). By introducing a model taking into account real-world optical and electronic responses of our setup and properly choosing the rotation angles (φ, θ), we have obtained a worst-case scenario certified min-entropy of (2.4 ± 0.5)%. This corresponds to a random bits throughput of 8.4 kHz in a non-optimized experimental configuration. Optimizing the acquisition parameters of an improved setup, we estimate that an overall throughput of 80 kHz is easily reachable.

18. Integration of single photon entanglement on a chip (Nicolò Leone, Stefano Azzini)

Single photon entanglement involves two degrees of freedom of the same photon. In a recent work, we have proven that SPE state of momentum and polarization con be obtained from attenuated sources like lasers, LEDs and halogen lamps. To test the presence of the entanglement at the single photon level, a Bell test in the CHSH form is carried out (Fig. 31 a,b). Here, the generated SPE state is measured in 2 different orthogonal basis of momentum and polarization by exploiting single photon avalanche diodes (SPADs). This measurement procedure is divided in two distinct stages. Firstly, we rotate the degrees of freedom of the SPE state by using unitary rotations R_φ and R_θ defined by a couple of angles (φ, θ). Then, the state is projected over the four fundamental states composing the Hilbert space: |0V>, |0H>, |1V>, |1H>, where |0> and |1> refer to the momentum degree of freedom, while |V>, and |H> refer to the polarization degree of freedom, with obvious meaning of the letters. Indeed, it can be mathematically demonstrated that measuring in a rotated basis is analogous to rotate the considered state and measure it in the fundamental basis. By choosing 4 couples of angles (φ, θ),(φ', θ),(φ, θ'),(φ', θ'), we can define the correlation function $S(\varphi, \varphi', \theta, \theta')$, that is based on the measurement outcomes. The S function can be used as a witness of entanglement: if $S(\varphi, \varphi', \theta, \theta')$|>2 for a particular choice of the angles $(\varphi, \varphi', \theta, \theta')$, then the entanglement between the degrees of freedom is present. Now we are characterizing a silicon-based photonic chip designed to integrate both the stages of generation of SPE states as well as the stages of the rotations needed for performing the Bell test. Since working on-chip with the polarization is particularly challenging, we chose instead to use the propagation mode of the light in the waveguides as one degree of freedom. Indeed, mode converters and mode-selective directional couplers have been developed through years, in our same group as well. As second degree of freedom, the momentum is still used. As an example, we report here the integrated structure that allows controlling the momentum rotation. An integrated Mach Zehnder interferometer was designed to obtain the rotation by exploiting the thermo-optics coefficient of the material (silicon nitride in our case). Indeed, a variation of temperature in one of the interferometer's arms, induced by heat dissipation due to Joule effect from a metal heater located on top of the waveguide, causes a variation of the guided modes effective index. This results in a phase delay between the two arms, which in turn causes a variation of the interference fringes, thus enabling the rotation. A preliminary characterization of the fabricated structure is reported in Fig. 32 and Fig. 33. In Fig. 32, the spectral response of one output port of the interferometer as a function of the wavelength for different values of voltage applied to the metal heater (0-8 V) is shown. It can be observed that the intensity decreases by increasing the applied voltage. The latter is highlighted in Fig. 33 where the intensity is reported as a function of the voltage for a specific wavelength ($\lambda = 808nm$): in red a sinusoidal fit appears to be in good agreement with the experimental data (blue dots). This confirms that our momentum rotation stage works as expected.

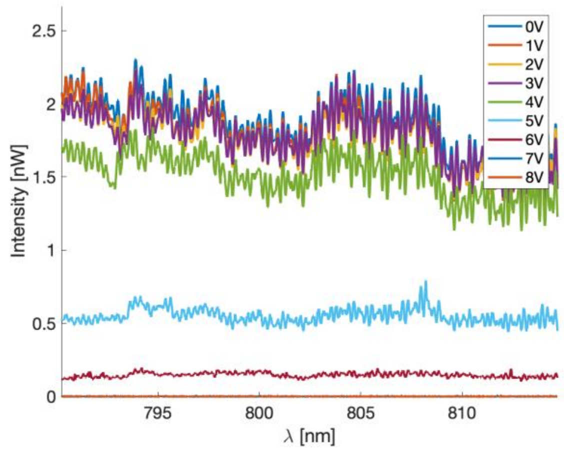

Figure 32: *Intensity (nW) of one output of the integrated Mach Zehnder interferometer under test as a function of the wavelength (nm) for different values of voltage applied (0-8V) to the metal heater of the interferometer. For all the involved wavelengths, the intensity decreases as a function of the voltage, because of the interference behavior.*

The successful integration of the SPE setup will enable interesting new applications in the field of quantum communications. For example, a cheap and integrated QRNG certified by SPE should be feasible. This device could find use in Internet of Things applications thanks to its compactness and cheapness. Validated the chip structure, another possible application consists in a novel quantum key distribution QKD protocol: Alice and Bob can exploit the SPE non-classical correlations to securely generate a shared private key applying BB84-like or more complex QKD protocols. So far, such kind of commercial quantum communication systems are implemented using bulky optical elements but the miniaturization and low-cost of a mass-produced photonic chips are key aspects for creating commercial devices with widespread diffusion.

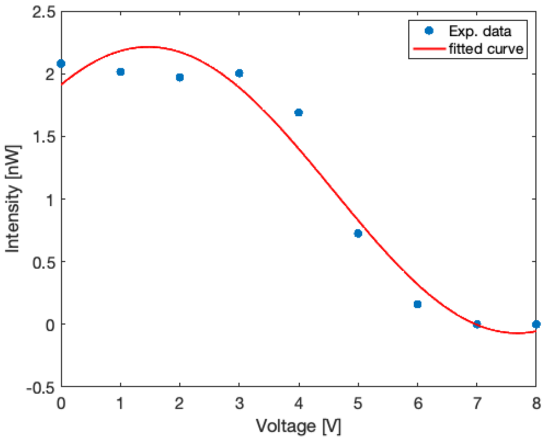

Figure 33: *Details of Figure 1 for ($\lambda = 808nm$): intensity (blue dots) detected at one of the outputs of the interferometer as a function of the voltage applied to the metal heater (0-8V). The red curve is a sinusoidal fit having equation: $I_0 sin(\omega V + \varphi) + I_1$.*

19. Cellulose-based nanomaterials (Marina Scarpa, Paolo Bettotti, Elvira D'Amato, Johanna Mae Indias, Federico Baldi)

Some natural molecules are able to behave as building blocks of materials with remarkable properties and functions. These molecules are willing to form hierarchical structures which bridge macroscale to molecular features, passing through fundamental structural elements whose dimension is within the nanoscale. In this regard, nanoscience and nanotechnology have to learn from nature to design structures, which have related analogs in biological materials, or to isolate nano structures already present in nature and arrange them to obtain innovative and environmentally friendly materials. The nanoscale elements forming the cellulose structure (i.e. nanocrystals and nanofibers) are among the most promising natural materials, since they are easily obtained from vegetables and offer a wide spectrum of possible applications.
In particular, we have developed procedures to isolate nanocrystals and nanofibers from the macroscopic cellulosic fibers by removing the amorphous domains. Cellulose nanocrystals are rigid sticks few hundreds nm long and with a cross section of about 10-20 nm^2. Their surface chemistry is flexible and, upon proper surface functionalization, large amount of surface charge can be imparted onto specific crystalline planes. Thus, the electrostatic interactions between the charge bearing groups and the water environment in which they are dissolved permit to tune the material properties and to realize materials spanning either liquid, gel as well as solid state. These materials have proved to be effective to fabricate membranes with selective gas barrier properties or hydrogels (Fig. 34).

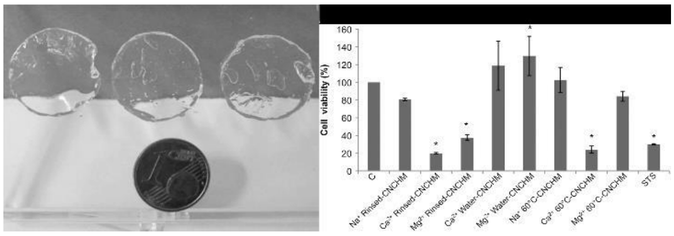

Figure 34 *Nanocellulose gel patches; (right) Cell viability measured by washing the sample with different protocols. Untreated cells were used as control, first column.*

Since 2019, we are exploring the possibility to recover cellulose-based high benefit products from agri-food wastes and to obtain hierarchical alignment of cellulose structures fabricated from pampas grass (Fig. 35).

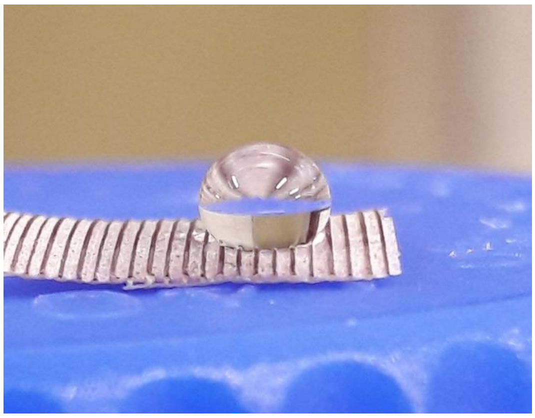

Figure 35: *A drop of water on a cellulose scaffold of pampas grass. (By Federico Baldi)*

For more info:

Nanoscience Laboratory
Department of Physics
University of Trento
via Sommarive 14
38123 Povo- Trento (Italy)
http://nanolab.physics.unitn.it/

Laboratory assistant
Dr. Chiara Rindone
email chiara.rindone@unitn.it
phone +39 0461 283172